International Journal of Thermal Sciences 158 (2020) 106542

Contents lists available at ScienceDirect

International Journal of Thermal Sciences

journal homepage: http://www.elsevier.com/locate/ijts

Shape optimization of inclined hole for enhanced film-cooling performance using discrete adjoint method

Aziz Madrane [a], Haichao An [a], Jiazhen Leng [a], Megan Schaenzer [b], Minh Quan Pham [b], Genevieve Bourgeois [b], Ali Shanian [b], Damiano Pasini [a,*]

[a] Department of Mechanical Engineering, McGill University, Montreal, QC H3A 2T8, Canada
[b] Siemens Power and Gas, Dorval, QC H9P 1A5, Canada

ARTICLE INFO

Keywords:
Shape optimization
Film cooling
Cooling effectiveness
Adjoint method
Method of moving asymptotes

ABSTRACT

This paper presents a gradient-based framework to optimize the film-cooling performance of heat bearing components in gas turbines. We examine a representative periodic component with very low porosity (below 1%) and optimize the shape of an inclined hole on the wall of a combustor for maximum cooling effectiveness, here defined as the normalized average decrease of downstream temperature. The shape boundary of the hole is parameterized using the coordinates of its control points here describing the design variables. Geometric constraints are introduced on the void area, symmetry relations and relative motion between planes along the line of extrusion. The cooling effectiveness is numerically evaluated through a RANS (Reynolds-Averaged Navier-Stokes)-based computational fluid dynamics (CFD) analysis. The Method of Moving Asymptotes (MMA) is adopted as the optimizer, with gradients computed using the adjoint method. Nine case studies with initial hole geometry of circular and elliptical shape as well as various inclination angles converge to a family of V-shapes that achieve more than 120% increase in cooling effectiveness. The automation of the workflow presented in this paper can be implemented in CFD-based optimization of other single and multi-objectives problems.

1. Introduction

Widely used in gas turbines, film cooling is an effective strategy to actively regulate the temperature of a component and protect it from the hot mainstream gas [5]. In film cooling, the cool air is injected on the surface to provide a protective film which helps maintain an acceptable temperature level on the surface, guarding the turbine component from failure. The efficiency of film cooling is strongly influenced by the shape of the injection hole, among other factors including blowing ratio, density ratio of coolant to hot gas, and turbulent intensity of free stream. Tailoring the shape boundary of the cooling hole has been shown effective in improving film-cooling efficiency [1,6,7,12–15,19,21,22,30–32].

The typical goal of the film-cooling problem in gas turbines is to optimize the geometry of the hole for maximum cooling effectiveness. Depending on the size of the problem, which is determined by the number of design variables defining the hole shape, various algorithms have been applied in the literature. Both evolutionary and gradient-based algorithms have been used for shape optimization of film cooling problems. The former rely on random perturbations of a single or a population of designs, which are updated with respect to a certain evolution criterion [27]. They usually do not require the evaluation of the gradients and can possibly avoid trapping into a local optimum; yet the number of objective function evaluations to perform can be very large, especially when the number of design variables increases, thus limiting their use in CFD-based optimization. Gradient-based algorithms, on the other hand, require the computation of the gradients or sensitivity of the objective function with respect to the design variables for the iterative update of a design solution, and the optimized designs are often local optima [20]. Their computational cost for small scale problems, where the gradient can be solved numerically using finite-difference or more efficient schemes, e.g. optimality conditions of the Lagrangian function, is well below than that required with evolutionary algorithms. Efforts exist in the literature to improve the tradeoff between accuracy and overhead, as reported in a recent review on aerodynamic shape optimization [26]. These include mixed algorithms using a bi- or multi-level approach that involves first the development and then the optimization of a CFD-based surrogate model [10]. While surrogate models do contribute to lowering the computational cost, their

* Corresponding author.
E-mail address: damiano.pasini@mcgill.ca (D. Pasini).

https://doi.org/10.1016/j.ijthermalsci.2020.106542
Received 9 September 2019; Received in revised form 22 April 2020; Accepted 8 July 2020
Available online 25 July 2020

Nomenclature

Acronyms

CFD	Computational Fluid Dynamics
FFD	Free Form Deformation
MMA	Method of Moving Asymptotes
RANS	Reynolds Averaged Navier Stokes
RBF	Radial Basis Function
SST	Shear Stress Transport

Greek symbols

α	Extrusion angle [°]
η	Cooling effectiveness [−]
ρ	Cooling air density $[kg/m^3]$
ν	Kinematic viscosity of the fluid $[m^2/s]$
τ_w	Wall shear stress $[N/m^2]$

Roman symbols

$\dot{m}$	Mass flow rate through the hole $[kg/s]$
A	Area $[m^2]$
C_D	Discharge coefficient [−]
D_R	Density ratio [−]
M	Blowing ratio [−]
M_a	Mach number [−]
P	Pressure $[Pa]$
P_r	Cooling performance [−]
R_e	Reynolds number [−]
T	Temperature $[K]$
T_I	Turbulence intensity [−]
V	Velocity $[m/s]$
y	Height of the first cell from the wall $[m]$
y^+	Normalized wall coordinate [−]

Subscripts

cold	Cold wall
hole	Hole
hot	Hot wall
jet	Jet flow into the hole
wall	Hot wall area
$wall_{avg}$	Area average of the hot wall

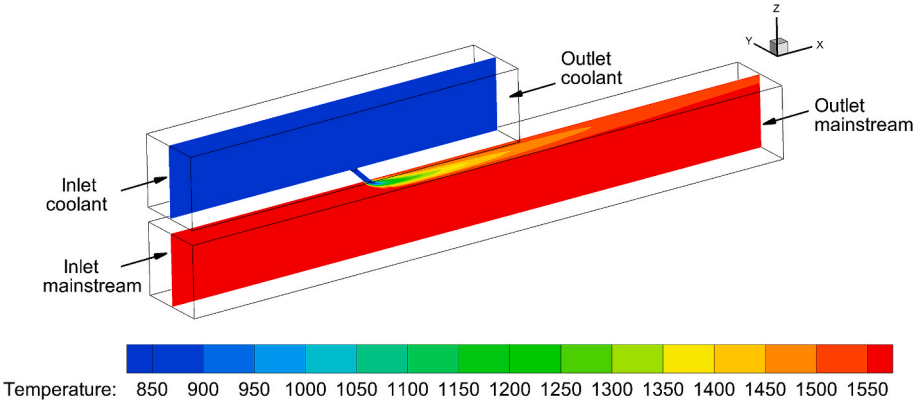

Fig. 1. Temperature distribution on the lateral mid plane of the hot and cold walls.

accuracy might not be always satisfactory.

It has been shown that intuitive design modifications of cooling holes can significantly enhance the film cooling performance. These approaches do not involves any optimization formulation; rather they resort to basic design alterations of standard cylindrical holes, typically obtained by enlarging the exit area [14], switching the injection pattern [15,22], adopting multi-level network or curved shape through the thickness [6,32], and utilizing staggered pattern [1]. Sequential programming has been recently used to optimize the film-cooling of a fan-shaped hole with geometry described by three variables, the injection angle, the lateral expansion angle and the ratio of length-to-diameter [12]. A fourth variable, i.e. the forward expansion angle of the hole, was then considered in a subsequent work [13]. For the cooling system design of a gas turbine blade, the locations and radii of a series of circular holes was optimized using a genetic algorithm (GA) and a conjugate heat transfer approach [21]. GA was also used to optimize the nonuniform impingement cooling of variable-diameter jet holes [7]. Another application of GA was the film-cooling optimization of fan-shaped holes in a rotating blade with three design variables [19]. More recently, a surrogate model using a radial basis function neural network was coupled with GA to optimize the film-cooling optimization of a fan-shaped hole [30]. A common feature of the above contributions is the low number of design variables, e.g. the radius of a circular hole, or the small size of enumeration, factors that favor the use of evolutionary algorithms [7,19,21] or mixed algorithms through surrogate modeling [12,13,30]. A recent work employed a gradient-based algorithm to optimize the 2D shape of the internal cooling passages in a guide vane modeled by Bazier curves [31]. This approach models the shape boundary of the hole with a smaller number of design variables for less computationally costly finite element method. Despite promising, this work cannot capitalize on the greater gain in film-cooling performance that could be obtained by parametrizing the shape boundary of the hole with a larger number of design variables capable of describing any generic shapes.

This work focuses on the shape optimization of a single cooling hole whose shape boundary is parameterized through the coordinates of the control points. We adopt a gradient-based scheme to handle a larger number of design variables, about ten times larger than that in previous studies using evolutionary or mixed algorithms, [12,13,19,30]. Distinct from others using a similar approach [31], our work allows greater variation of the hole, whose shape boundary is described by the coordinates of its control points rather than the design variables of certain families of curves. The adjoint method [2,4,8,11] is here implemented with a discrete formulation, where the augmented cost function is discretized before variations are taken, as opposed to a continuous formulation, where the adoption of different levels of truncation error

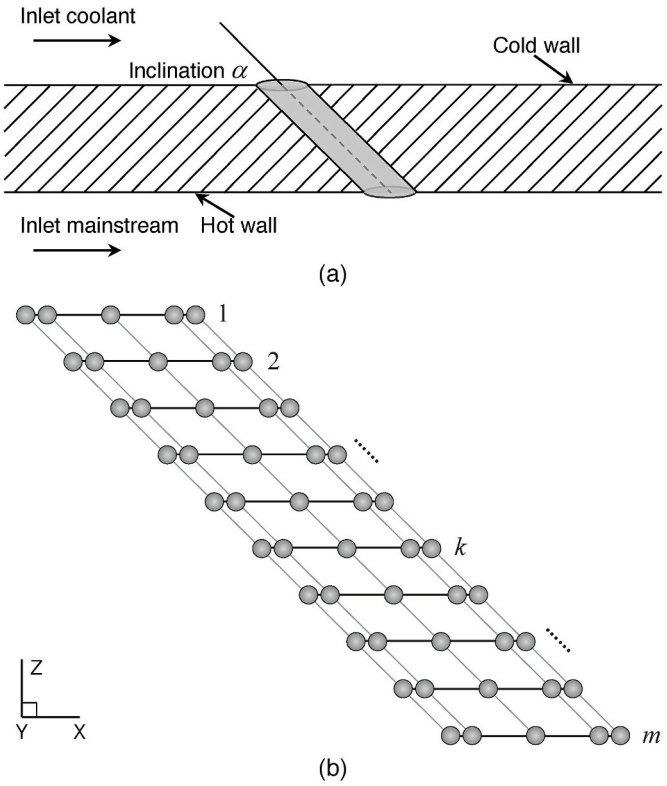

Fig. 2. Shape description of the inclined hole: (a) Side view of the material wall with the in-plane shape of the hole, (b) Side view of the inclined hole with its control points at each section.

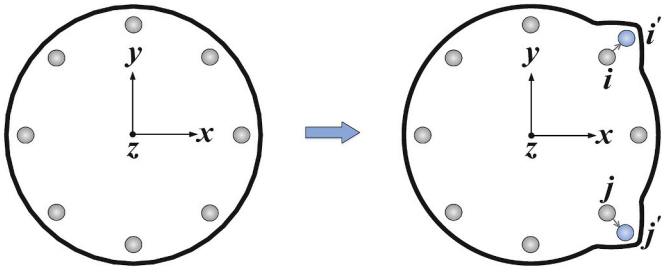

Fig. 3. Symmetry constraint of hole shape in *x*-*y* plane about *x* axis.

might degrade results accuracy [25]. Section 2 of the paper presents the problem formulation along with the definition of the objective function and design variables, as well as the implementation of constraints. Section 3 explains the optimization framework with a description of the numerical solvers and the grid deformation technique. Section 4 shows the optimization results for multiple case studies, followed by a discussion that compares the relative cooling performance of the optimized hole shapes. The last section concludes the paper with a set of suggestions for future work.

2. Problem formulation

2.1. Objective function and design variables

Fig. 1 shows a typical temperature pattern generated by film cooling on a hot wall. The downstream temperature drops significantly near the hole of the inlet secondary cooling air, while it recovers at a certain distance away from the hole.

The performance of the film cooling can be assessed through the cooling effectiveness, a normalized measure of the temperature reduction on the adiabatic hot wall. The cooling effectiveness is calculated as

$$\eta = \frac{T_{hot} - T_{wall_{avg}}}{T_{hot} - T_{cold}} \tag{1}$$

$T_{wall_{avg}}$ is taken as the average over the entirety of the hot wall. The cooling effectiveness is used to determine the thermal performance of the shape. Values of $\eta = 1$ indicate that the cooling has reached its maximum potential of the cold flow. High values of η typically occur directly downstream of the injection holes, and η drops until the hot wall recovers the freestream hot temperature ($\eta = 0$) further away from the hole. The goal is then to maximize η, and it is customary to formulate the optimization problem as a minimization one, i.e. the merit function of $1/\eta$ is adopted as objective function.

For this application, the cooling effectiveness is not the only metric of interest. For turbine applications, it is generally desirable to reduce the mass flow rate of cooling air through the hole to reduce the amount of air that is bled from the combustion process. This metric is non-dimensionalized by considering the discharge coefficient, C_D (dimensionless), which is calculated as follows:

$$C_D = \frac{\dot{m}}{A_{hole}\sqrt{2\Delta P \rho}} \tag{2}$$

In this work, a combined dimensionless metric with the cooling effectiveness and discharge coefficient is used to evaluate the efficiency of each hole design. The metric, P_r, is computed as follows:

$$P_r = \frac{\eta}{C_D}\frac{A_{wall}}{A_{hole}} \tag{3}$$

In this paper, the metric will be referred to as the cooling performance. It is a normalized parameter that can also be used to directly compare different geometries.

Fig. 2 illustrates the shape of the inclined hole. As shown in Fig. 2 (a), the hole is generated by extruding the shape of the in-plane cross-section through the thickness of the wall. Fig. 2(b) is a zoom-in of the hole geometry here described by the coordinates of the control points in the *x*-*y* plane and by *m* cross-sections evenly distributed through the thickness of the wall. A difference from previous works [12,13,19,30] is that the lateral expansion is not included in the extrusion, because the technology (laser cutting) adopted by the industrial partner limits the hole generation to extruded shapes only; hence the *m* cross-section shapes are congruent in a given hole.

As per the definition of the constraints, a number of conditions apply. First the cooling hole area should remain constant, a condition that translates to a prescribed value of porosity, denoted by C_k for each of *m* cross-sections. In addition, the shape of the hole in the *x*-*y* plane should be symmetric about the *x* axis, hence symmetry relations are enforced on every cross-section. The above constraints are casted into the following problem formulation

$$\begin{cases} \min\limits_{\boldsymbol{x}_p} & 1/\eta \\ \text{subject to} & C_k = 0 \\ & H_k = 0 \\ & \underline{\boldsymbol{x}}_{p,k} \le \boldsymbol{x}_{p,k} \le \overline{\boldsymbol{x}}_{p,k}, \quad k = 1, \ldots, m \end{cases} \tag{4}$$

where $\eta = \eta(\boldsymbol{x}_p)$ is the cooling effectiveness function, $\boldsymbol{x}_p$ is the vector of the design variables, $C_k = Area_k - Area_0$ and H_k are the geometric constraints on the cooling area and shape relation symmetry, $\underline{\boldsymbol{x}}_{p,k}$ and $\overline{\boldsymbol{x}}_{p,k}$ are the lower and upper bounds for the design variables respectively, enforced on the *k*-th of *m* cross-sections along *z*-direction in Fig. 2(b).

2.2. Implementation of constraints

The symmetry constraint of the hole shape is proposed by the industry partner for the consideration of laser cutting technology. Fig. 3

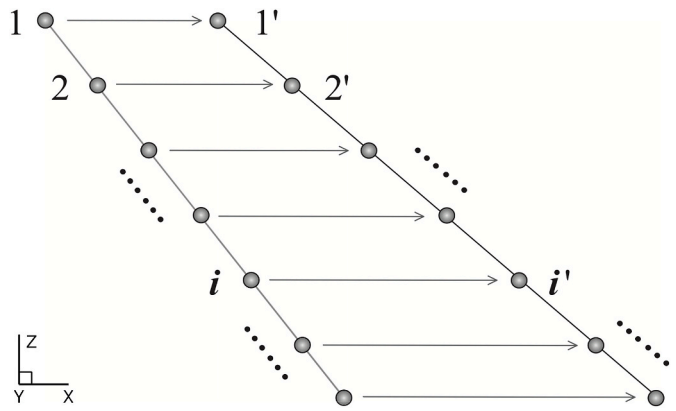

Fig. 4. Shift of the control points.

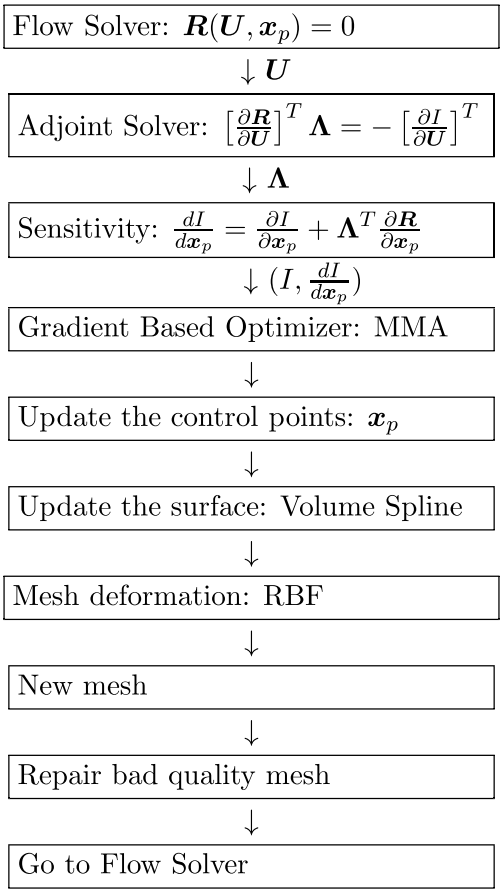

Fig. 5. Flowchart of the film-cooling optimization framework.

shows the symmetry condition of a hole shape in the *x*-*y* plane about the *x* axis, where *i* and *j* represent a pair of reflected control points. We use (x_i, y_i, z_i) to describe the original position of a general control point *i*, and $(x_{i'}, y_{i'}, z_{i'})$ for its new position. The control points of the initial in-plane shape on the left of Fig. 3 are symmetric with respect to the *x* axis. To preserve mesh deformation symmetry in the *x*-*y* plane, we imposed the condition:

$$H_k = 0 \Rightarrow \begin{pmatrix} x_i - x_j \\ y_i + y_j \\ z_i - z_j \end{pmatrix}_k = \begin{pmatrix} 0 \\ 0 \\ 0 \end{pmatrix} \quad \text{and} \quad \begin{pmatrix} x_{i'} - x_{j'} \\ y_{i'} + y_{j'} \\ z_{i'} - z_{j'} \end{pmatrix}_k = \begin{pmatrix} 0 \\ 0 \\ 0 \end{pmatrix} \; k = 1, \ldots, m \tag{5}$$

Because the congruency of all *m* cross-sections in Fig. 2(b) imposes equal in-plane shift of the control points, the number of independent design variables reduces significantly.

The constraint on the area of the hole is expressed in a relaxed form through the inequalities

$$Area_0(1 - \varepsilon_1) \leq Area_k \leq Area_0(1 + \varepsilon_2) \tag{6}$$

where ε_1 and ε_2 are relaxation parameters, e.g. 0.05.

The linear extrusion of the hole at an inclination angle α imposes a further constraint on the control points of each cross-section shape. As illustrated in Fig. 4, although changes in the inclination angle are allowed, the control points between cross-sections should remain collinear. This translates into a constraint on the *z* coordinate of the control points $z_j = z_{j'}$.

The set of constraints on the *x*, *y* and *z* coordinates of the control points is thus given by:

$$\begin{cases} \frac{z_2 - z_1}{x_2 - x_1} = \cdots = \frac{z_i - z_1}{x_i - x_1} = \cdots = \tan(\alpha) \\ \frac{z_{2'} - z_{1'}}{x_{2'} - x_{1'}} = \cdots = \frac{z_{i'} - z_{1'}}{x_{i'} - x_{1'}} = \cdots = \tan(\alpha') \\ y_{1'} - y_1 = \cdots = y_{i'} - y_i = \cdots = \Delta d_y \end{cases} \tag{7}$$

where α' is the inclination angle after the shift of the control points and Δd_y the increment of the *y*-component.

If the inclination angle is given, Eq. (7) simplifies to:

$$\begin{cases} x_{1'} - x_1 = \cdots = x_{i'} - x_i = \cdots = \Delta d_x \\ y_{1'} - y_1 = \cdots = y_{i'} - y_i = \cdots = \Delta d_y \\ z_{1'} - z_1 = \cdots = z_{i'} - z_i = \cdots = 0 \end{cases} \tag{8}$$

where Δd_x is the increment of the *x*-component.

3. Optimization framework

Fig. 5 illustrates the shape optimization flowchart for cooling effectiveness, which is automated through a Python script. First the flow solver determines the flow variable $\boldsymbol{U}$ of the Navier-Stokes equations and evaluates the objective function, i.e. the cooling effectiveness. Then $\boldsymbol{U}$ is passed to the discrete adjoint solver that solves the Lagrangian multiplier $\boldsymbol{\Lambda}$ required to evaluate the sensitivity of $\boldsymbol{U}$ with respect to the design variables $\boldsymbol{x}_p$. The method of moving asymptotes is used to update the design variables, i.e. the coordinates of the control points [28,29]. To avoid the computational cost of remeshing, the shift of the control points governs the deformation of the finite volume mesh. The update of the mesh grid points is performed in two steps: a volume spline interpolation of the control points is used to update the surface of the hole, and Radial Basis Functions (RBF) are used to update the volume mesh enclosed by the hole shape. A module for mesh quality control follows the RBF interpolation to repair distorted elements with large deformation.

3.1. Numerical analysis

This section describes the elements that underpin the CFD simulation: flow solver, adjoint solver and mesh deformation. Among those, the key component is the discrete adjoint solver, which reduces the cost of the gradient evaluation, because it is practically independent from the number of design variables, as opposed to other methods that use finite-difference or complex step.

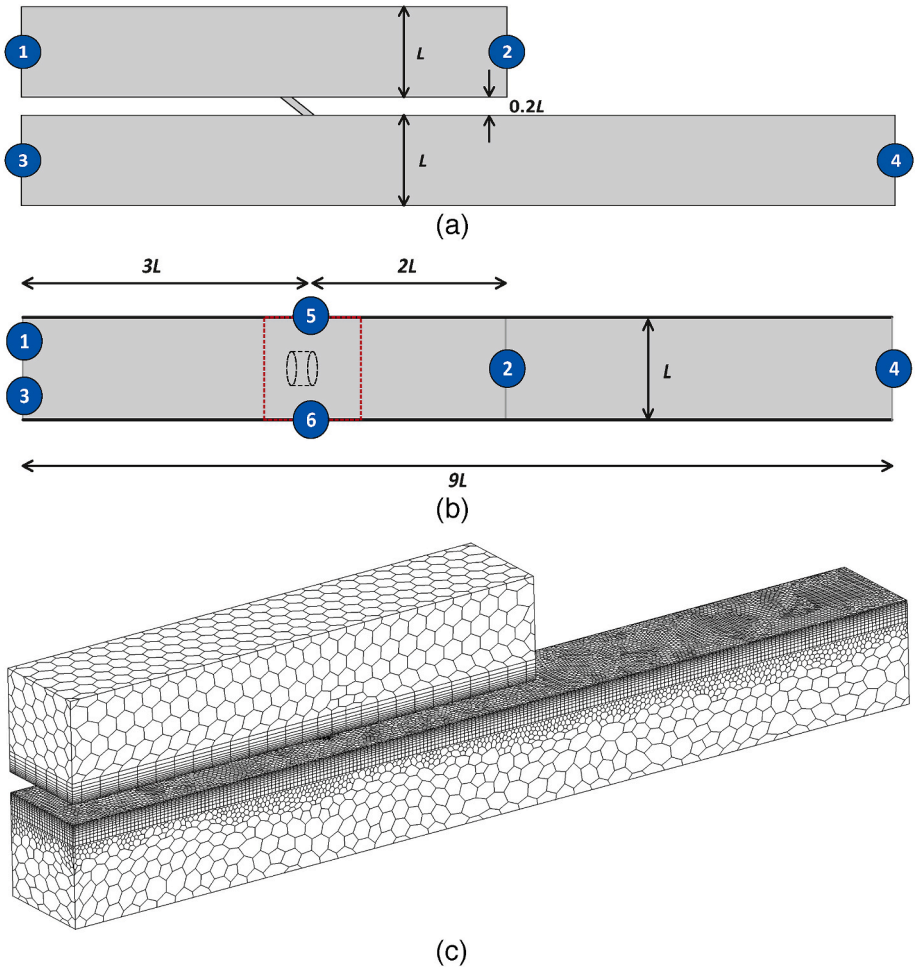

Fig. 6. CFD model of a circular hole with $\alpha = 45°$, $L = 5mm$: (a) Side view with four markers of the boundaries of the solution domain, (b) Top view with six markers of the boundaries of the solution domain, (c) Finite volume mesh.

Table 1
Boundary conditions for CFD simulations.

Boundary	Type	$V(m/s)$	Total P (Pa)	Total T (K)
1	Stagnation inlet	–	84509	800
2	Pressure outlet	–	78558	800
3	Velocity inlet	60	–	1600
4	Pressure outlet	–	4510[a]	1600
5	Periodic	–	–	–
6	Periodic	–	–	–

[a] Static Pressure.

3.1.1. Flow solver

The flow solver solves the compressible Reynolds-averaged Navier-Stokes equations with a cell-center based finite volume discretization on hybrid grids of prismatic, pyramidal, hexahedral and tetrahedral elements (see Fig. 6). The Navier-Stokes equations for the three-dimensional case can be written in conservative form as

$$\frac{\partial}{\partial t}\int_V \boldsymbol{U} dV = -\int_{\partial V} \overline{\overline{\boldsymbol{F}}}\cdot\boldsymbol{n} dS \tag{9}$$

where $\boldsymbol{U}$ is the vector of the conserved variables. V denotes an arbitrary control volume with the boundary ∂V and the outer normal $\boldsymbol{n}$. The flux density tensor $\overline{\overline{\boldsymbol{F}}}$ consists of inviscid and viscous contributions flux vectors in the three coordinate directions:

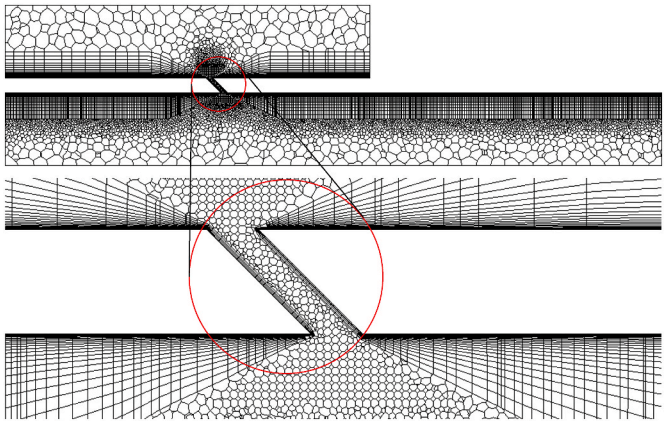

Fig. 7. CFD model of a circular hole with $\alpha = 45°$, $L = 5mm$: cut view of the simulation mesh showing the prismatic layer.

$$\overline{\overline{\boldsymbol{F}}} = \sum_{i=1}^{3}(\boldsymbol{F}_{c,i} + \boldsymbol{F}_{v,i})\cdot\boldsymbol{e}_{x_i} \tag{10}$$

As for the discretization, the temporal change of the conservative variables $\boldsymbol{U}$ can be related to the flux over the control volume boundary ∂V and derived from Eq. (9) as

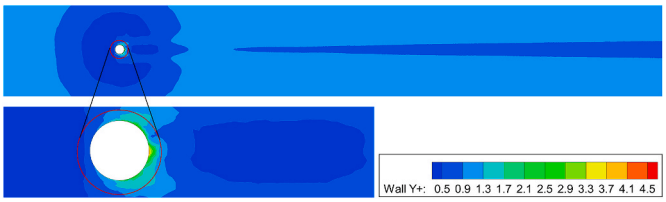

Fig. 8. CFD model of a circular hole with $\alpha = 45°$, $L = 5mm$: the distribution of y^+ of the computational mesh of the hot wall.

Table 2
Main characteristics of the simulations in the mesh sensitivity study.

Run	Grid	Number of Cells	$V_{jet}(m/s)$	M	C_D	η
A	C	105387	80.58	2.68	0.73	0.0186
B	M	145228	81.06	2.70	0.74	0.0184
C	F	501679	80.84	2.69	0.73	0.0169

Table 3
Operating conditions of the CFD simulations.

Physical quantity			
Kinematic viscosity of the fluid	ν	1.716×10^{-5}	(m^2/s)
Hole diameter	d	5.0×10^{-4}	(m)
Inlet velocity	V_{hot}	60	(m/s)
Inlet velocity (target velocity)	V_{cold}	30	(m/s)
Turbulence intensity	T_I	0.01	(–)

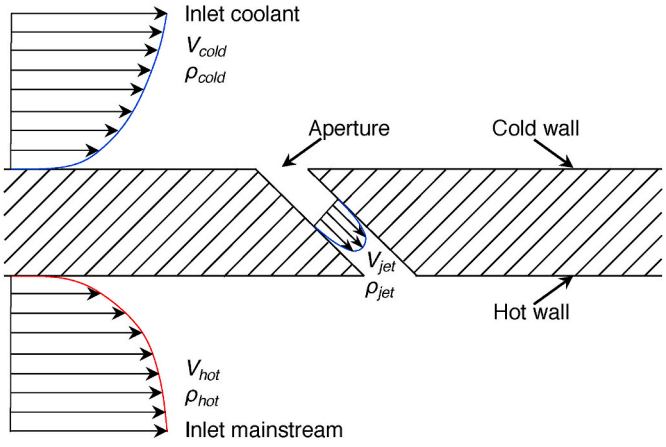

Fig. 9. Definition of the different velocities and mass densities for the description of the flow.

$$\frac{\partial}{\partial t}\boldsymbol{U}\int_V dV = -\int_{\partial V}\overline{\overline{\boldsymbol{F}}}\cdot\boldsymbol{n}dS \quad in \quad D \tag{11}$$

For a control volume fixed in time and space, Eq. (11) can be written as

$$V\frac{\partial \boldsymbol{U}}{\partial t} + \boldsymbol{R}(\boldsymbol{U}) = 0 \quad in \quad D \tag{12}$$

where V is the volume of the control volume, $\boldsymbol{R}(\boldsymbol{U})$ is the residual comprised of the convective and dissipative fluxes, and D is the computational domain.

The spatial discretization of convective flux of this work is the Roe scheme [23]. The time integration is an implicit backward Euler scheme. For turbulence modeling, the Menter's Shear Stress Transport (SST) model [18] is adopted. The transport equation for the turbulence kinetic energy (K) and the specific dissipation of turbulence (ω) read in differential form [18]. The spatial discretization of the two equations K and ω is decoupled from Eq. (9). After numerical testing, we selected five layers of the mutltigrid mesh to accelerate the convergence of the RANS solution.

3.1.2. Adjoint solver

In this work, the cost function I is $1/\eta$, the reciprocal of the cooling effectiveness defined by Eq. (1). The gradient of the cost function $I = I(\boldsymbol{U}(\boldsymbol{x}_p),\boldsymbol{x}_p)$, where $\boldsymbol{U}$ is the vector of the flow variables that depends on the design variables $\boldsymbol{x}_p$, is given by

$$\frac{dI}{d\boldsymbol{x}_p} = \frac{\partial I}{\partial \boldsymbol{x}_p} + \frac{\partial I}{\partial \boldsymbol{U}}\frac{\partial \boldsymbol{U}}{\partial \boldsymbol{x}_p} \tag{13}$$

To determine the sensitivity term $\partial \boldsymbol{U}/\partial \boldsymbol{x}_p$, the flow solution has to be usually computed for each design variable, a requirement that can become computationally expensive for a large number of variables. On the other hand, the adjoint approach decouples the gradient calculation of the cost function I of the flow variables $\boldsymbol{U}$ through the definition of the following Lagrangian function L:

$$L\left(\boldsymbol{U}(\boldsymbol{x}_p),\boldsymbol{x}_p,\boldsymbol{\Lambda}\right) = I\left(\boldsymbol{U}(\boldsymbol{x}_p),\boldsymbol{x}_p\right) + \boldsymbol{\Lambda}^T\boldsymbol{R}\left(\boldsymbol{U}(\boldsymbol{x}_p),\boldsymbol{x}_p\right) \tag{14}$$

Table 5
A summary of initial and optimal designs (Case 1 to 4).

Design cases	Initial Design	Case 1	Case 2	Case 3	Case 4
$(\varepsilon_1,\varepsilon_2,\alpha_0)$	–	$(0.05, 0.05, 45°)$	$(1.0, 0.05, 45°)$	$(0.05, 0.05, 45°)$	$(1.0, 0.05, 45°)$
A_{hole}, m^2	1.94439×10^{-7}	2.08603×10^{-7}	1.85125×10^{-7}	1.98703×10^{-7}	1.96428×10^{-7}
α	45°	45°	45°	30.69°	35.48°
η	0.018451	0.042122	0.042248	0.046888	0.048213
$\%\Delta A_{hole}$	0%	7.28%	− 4.79%	2.19%	1.02%
$\%\Delta\eta$	0%	128.29%	128.97%	154.12%	161.30%

Table 4
Parameter descriptions of the numerical studies.

	Case 1	Case 2	Case 3	Case 4	Case 5	Case 6
Initial Shape	Circular	Circular	Circular	Circular	Elliptical	Elliptical
Inclination Angle	$\alpha \equiv 45°$	$\alpha \equiv 45°$	$\alpha_0 = 45°$	$\alpha_0 = 45°$	$\alpha_0 = 45°$	$\alpha_0 = 45°$
Area Constraint	$\varepsilon_1 = \varepsilon_2 = 0.05$	$\varepsilon_1 = 1.0, \varepsilon_2 = 0.05$	$\varepsilon_1 = \varepsilon_2 = 0.05$	$\varepsilon_1 = 1.0, \varepsilon_2 = 0.05$	$\varepsilon_1 = \varepsilon_2 = 0.05$	$\varepsilon_1 = 1.0, \varepsilon_2 = 0.05$
Symmetry	Yes	Yes	Yes	Yes	Yes	Yes
	Case 7	Case 8	Case 9			
Initial Shape	Elliptical	Elliptical	Elliptical			
Inclination Angle	$\alpha_0 = 60°$	$\alpha_0 = 80°$	$\alpha_0 = 90°$			
Area Constraint	$\varepsilon_1 = 1.0, \varepsilon_2 = 0.05$	$\varepsilon_1 = 1.0, \varepsilon_2 = 0.05$	$\varepsilon_1 = 1.0, \varepsilon_2 = 0.05$			
Symmetry	Yes	Yes	Yes			

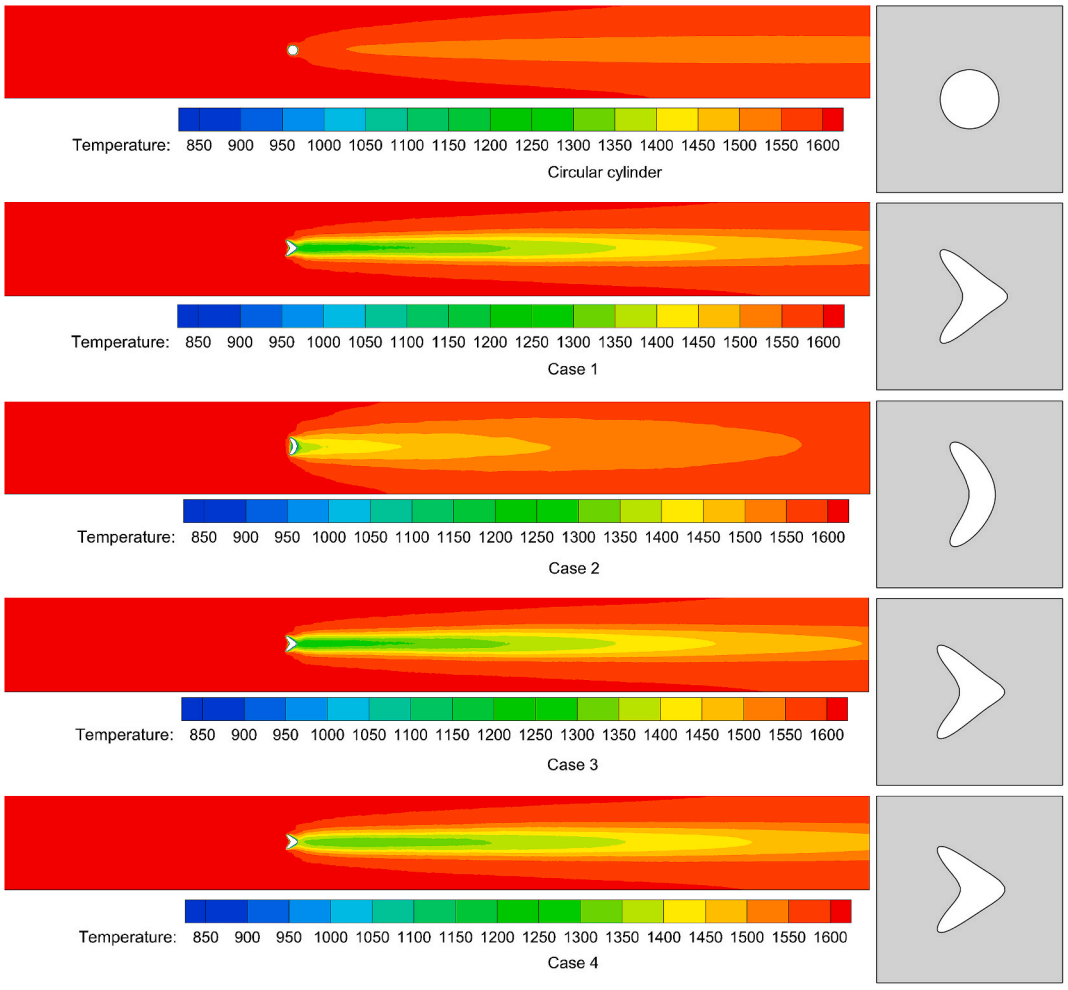

Fig. 10. Temperature on hot wall, initial design (circular cylinder) vs. optimal shapes (Case 1 to 4).

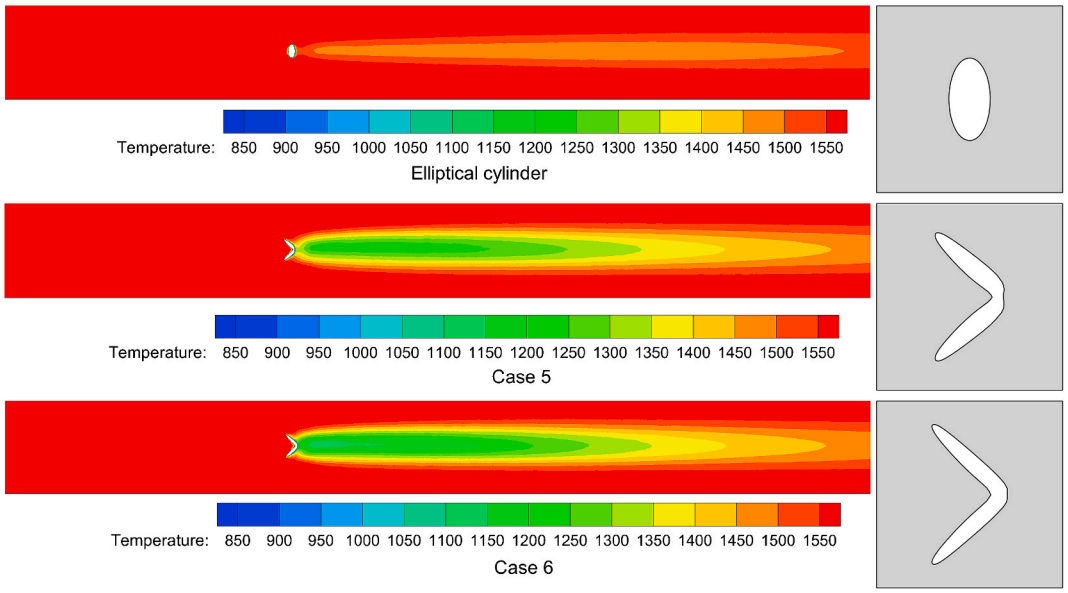

Fig. 11. Temperature on hot wall, initial design (elliptical cylinder) vs. optimal shapes (Cases 5 and 6).

Table 6
A summary of initial and optimal designs (Case 5 and 6).

Design cases	Initial Design	Case 5	Case 6
$(\varepsilon_1, \varepsilon_2, \alpha_0)$	–	$(0.05, 0.05, 45°)$	$(1.0, 0.05, 45°)$
A_{hole}, m^2	1.90744×10^{-7}	2.02456×10^{-7}	2.01120×10^{-7}
α	45°	45.41°	44.30°
η	0.029171	0.080888	0.087014
$\%\Delta A_{hole}$	0%	6.14%	5.44%
$\%\Delta\eta$	0%	177.23%	198.29%

where $\boldsymbol{R}$ is the flow residual and $\boldsymbol{\Lambda}$ is the Lagrangian multiplier. By taking the derivatives of the Lagrangian function, the first-order Karush-Kuhn-Tucker (KKT) conditions can be expressed as

$$\begin{cases} \boldsymbol{R}(\boldsymbol{U}, \boldsymbol{x}_p) = 0 & \text{Flow Solver} \\ \left[\frac{\partial \boldsymbol{R}}{\partial \boldsymbol{U}}\right]^T \boldsymbol{\Lambda} = -\left[\frac{\partial I}{\partial \boldsymbol{U}}\right]^T & \text{Adjoint Solver} \\ \frac{dI}{d\boldsymbol{x}_p} = \frac{\partial I}{\partial \boldsymbol{x}_p} + \boldsymbol{\Lambda}^T \frac{\partial \boldsymbol{R}}{\partial \boldsymbol{x}_p} & \text{Sensitivity} \end{cases} \tag{15}$$

The expression of the cost function gradient finally simplifies to

$$\frac{\partial L}{\partial \boldsymbol{x}_p} = \left[\frac{\partial I}{\partial \boldsymbol{x}_s} + \boldsymbol{\Lambda}^T \frac{\partial \boldsymbol{R}}{\partial \boldsymbol{x}_v} \frac{\partial \boldsymbol{x}_v}{\partial \boldsymbol{x}_s}\right] \frac{\partial \boldsymbol{x}_s}{\partial \boldsymbol{x}_p} \tag{16}$$

where the volume mesh points $\boldsymbol{x}_v(\boldsymbol{x}_s(\boldsymbol{x}_p))$ and the surface mesh points $\boldsymbol{x}_s$ are function of the control points $\boldsymbol{x}_p$ of the hole shape and $\partial \boldsymbol{x}_v / \partial \boldsymbol{x}_s$ is the mesh sensitivity. Therefore, given a solution $\boldsymbol{U}$ to the governing equation $\boldsymbol{R}(\boldsymbol{U}(\boldsymbol{x}_p), \boldsymbol{x}_p) = 0$ and the corresponding adjoint state $\boldsymbol{\Lambda}$, $\frac{dI}{d\boldsymbol{x}_p}$ can be computed at a cost independent of the number of parameter in $\boldsymbol{x}_p$. To update the finite volume mesh from the shift of the control points, the target surface defined by the control points should be updated first through the interpolation of the coordinates of the control points. To do so, we adopt here the Free Form Deformation (FFD) approach [24], a technique that uses a relatively small number of control points to manipulate the global shape of the hole. After the creation of the deformed target surface via FFD, the grid points of the deformed finite volume mesh defined on the target surface are updated through the use of a classic volume spline, which here describes a type of Radial Basis Functions (RBF) [9].

3.2. The Method of Moving Asymptotes

The method of moving asymptotes is a non-linear programming algorithm widely used for structural optimization problems having a large

Table 7
A summary of initial and optimal designs (Case 7 to 9).

Design cases	Initial Design	Case 7	Case 8	Case 9
$(\varepsilon_1, \varepsilon_2, \alpha_0)$	–	$(1, 0.05, 60°)$	$(1.0, 0.05, 80°)$	$(1.0, 0.05, 90°)$
A_{hole}, m^2	1.90744×10^{-7}	1.67693×10^{-7}	2.08603×10^{-7}	1.73968×10^{-7}
α	60°/80°/90°	60°	80°	90°
η	0.01475/0.00368/0.00641	0.058187	0.019939	0.0223742
$\%\Delta A_{hole}$	0%	− 12.02%	− 17.67%	− 8.60%
$\%\Delta\eta$	0%	294.30%	440.47%	248.88%

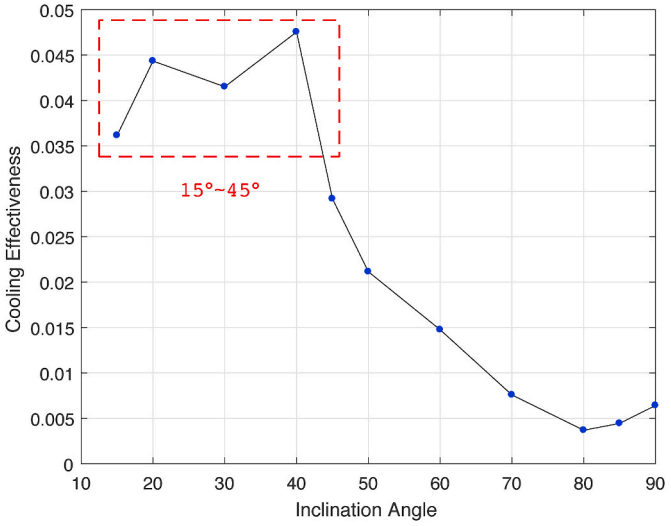

Fig. 13. CFD analysis results on cooling effectiveness with different inclination angles.

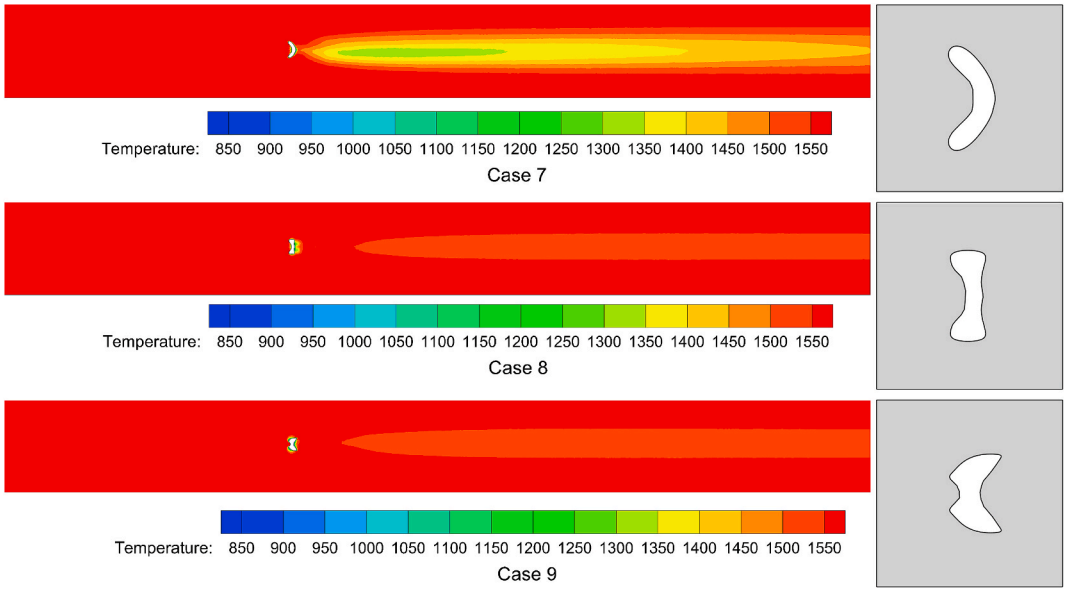

Fig. 12. Temperature on hot wall, optimal shapes (Case 7 to 9).

Table 8
Cooling performance comparison of the initial and optimized designs of nine cases.

	Cases	$V_{jet}(m/s)$	M	D_R	C_D	P_r
Initial shape,	(Circular cylinder, $\alpha_0 = 45°$)	81.06	2.70	2.00	0.74	28.79
Optimized shape,	Case 1	74.27	2.47	2.00	0.48	108.70
Optimized shape,	Case 2	74.09	2.46	2.00	0.67	76.54
Optimized shape,	Case 3	74.27	2.47	2.00	0.48	108.70
Optimized shape,	Case 4	77.49	2.58	2.00	0.57	95.91
Initial shape,	(Elliptical cylinder, $\alpha_0 = 45°$)	79.67	2.65	2.00	0.72	47.31
Optimized shape,	Case 5	74.53	2.48	2.00	0.70	127.81
Optimized shape,	Case 6	74.52	2.48	2.00	0.65	146.31
Initial shape,	(Elliptical cylinder, $\alpha_0 = 60°$)	82.26	2.47	2.00	0.92	18.79
Optimized shape,	Case 7	77.34	2.57	2.00	0.89	87.60
Initial shape,	(Elliptical cylinder, $\alpha_0 = 80°$)	76.55	2.55	2.00	0.98	4.41
Optimized shape,	Case 8	76.74	2.55	2.00	1.00	28.57
Initila shape,	(Elliptical cylinder, $\alpha_0 = 90°$)	71.06	2.36	2.00	0.90	8.36
Optimized shape,	Case 9	71.27	2.37	2.00	0.92	31.21

number of variables and constraints [28]. The design variable vector, $\boldsymbol{x}$, collects the components $x_j, j = 1, \ldots, n$ satisfying bound constraints $\underline{x}_j \le x_j \le \overline{x}_j$. The objective function is represented by $f_0(\boldsymbol{x})$ and $f_i(\boldsymbol{x})$, where m denotes inequality constraints of the form $f_i(\boldsymbol{x}) \le \widehat{f}_i$. The design variables are updated interactively by solving a strictly convex approximation of the original problem.

At iteration k, the subproblem $P^{(k)}$ consists of fraction form approximation $f_i^{(k)}$ for each $i = 0, 1, \ldots, m$:

$$f_i^{(k)}(\boldsymbol{x}) = r_i^{(k)} + \sum_{j=1}^{n}\left(\frac{p_{ij}^{(k)}}{U_j^{(k)} - x_j} + \frac{q_{ij}^{(k)}}{x_j - L_j^{(k)}}\right) \tag{17}$$

where

$$p_{ij}^{(k)} = \begin{cases} \left(U_j^{(k)} - x_j^{(k)}\right)^2 \partial f_i / \partial x_j, & \text{if } \partial f_i/\partial x_j > 0 \\ 0, & \text{if } \partial f_i/\partial x_j \le 0 \end{cases} \tag{18}$$

$$q_{ij}^{(k)} = \left\{0, \text{if } \partial f_i / \partial x_j \ge 0 - \left(x_j^{(k)} - L_j^{(k)}\right)^2 \partial f_i \Big/ \partial x_j, \text{if } \partial f_i / \partial x_j < 0\right. \tag{19}$$

$$r_i^{(k)} = f_i\left(\boldsymbol{x}^{(k)}\right) - \sum_{j=1}^{n}\left(\frac{p_{ij}^{(k)}}{U_j^{(k)} - x_j^{(k)}} + \frac{q_{ij}^{(k)}}{x_j^{(k)} - L_j^{(k)}}\right) \tag{20}$$

where all derivatives $\partial f_i/\partial x_j$ are evaluated at $\boldsymbol{x} = \boldsymbol{x}^{(k)}$.

Note that at iteration k, the design variable should be in a subinterval of $L_j^{(k)} < x_j < U_j^{(k)}$ with the bounds $U_j^{(k)}$ and $L_j^{(k)}$ dependent on k. The lower and upper bounds of the design variables in Eq. (4) are adopted as the initial value of L_j and U_j in Eqs. (17)–(20). The varying bounds are termed "moving asymptotes" in the eponymous algorithm.

It can be shown that Eq. (17) is a strictly convex approximation of the original problem and thus easy to solve. In our case, $\boldsymbol{x}$ is the design variable vector containing the coordinates of all control points of the hole shape, and the constraints are given in Section 2.1. The efficiency of the convex approximation of MMA is discussed in the literature [28]. Compared to a previous work that uses a globally convergent MMA (GCMMA) in 2D shape optimization [31], here we adopt the classical framework of MMA due to its simplicity and proved reduction in the computational cost imposed by our model, and implement the primal-dual iteration scheme [29] to solve the problem in MATLAB (MathWorks, Natick, MA).

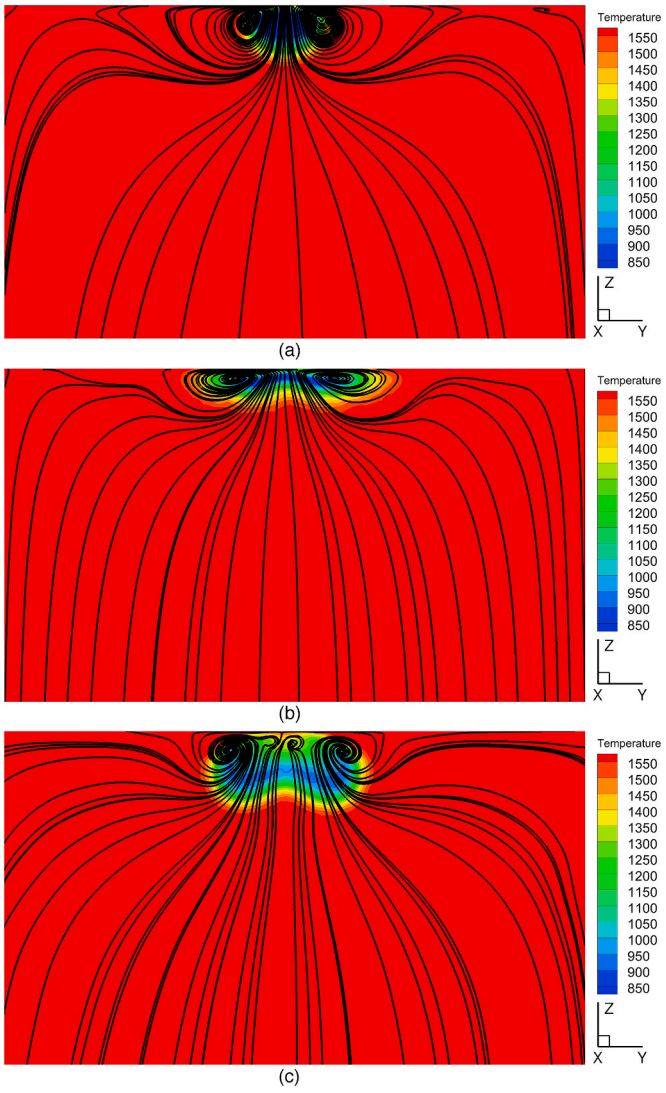

Fig. 14. Velocity vectors align with temperature contours in the y-z plane, $x = 3.0 \times 10^{-4}$: (a) Circular hole, (b) Case 6 (see Fig. 11), (c) Case 9 (see Fig. 12).

4. Application

4.1. Numerical case study: description and setup

We examine nine cases of shape optimization of an inclined hole to identify the optimal in-plane shape for maximum cooling effectiveness. A further parametric study locates the range of inclination angle for optimal cooling. Fig. 6 shows a representative CFD model describing the evaluation of the cooling effectiveness of an inclined hole. The side view in Fig. 6(a) and top view in Fig. 6(b) show the void shape and the faces with flow boundary conditions. The pressure conditions are chosen to attain a pressure drop of 2.5% across the boundaries 1 and 4. The

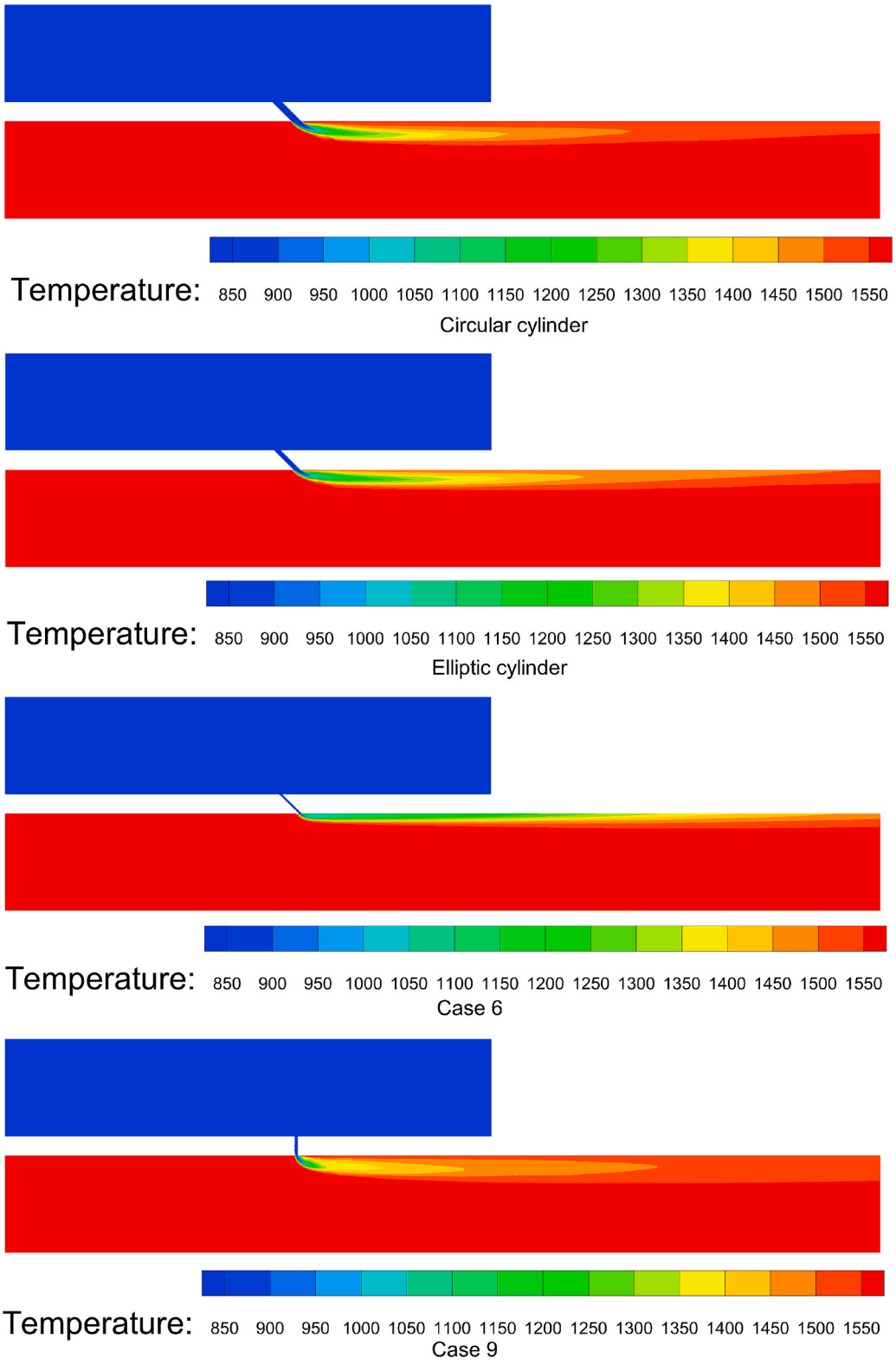

Fig. 15. Lateral view of temperature profiles of Circular hole, Elliptical hole, Case 6 and Case 9.

pressure on boundary 2 is specified to achieve a target velocity of 30 m/s in the cold (top) section of the domain. In addition, the operating pressure is specified to be 3.2 MPa, and the turbulence intensity and turbulent length scale on all inlets is specified to be 10% and 0.012 m, respectively. The M_a of the jet flow into the aperture is close to 0.2 while the R_e value obtained from the jet velocity and the hole diameter is 3306. A summary of the boundary conditions is given in Table 1. As advised by the industry partner, the porosity is set to a value below 1% , i.e. 0.25%. The shear stress transport (SST) turbulence model is typically used as a turbulence closure [18]. The SST model works by solving a turbulence/frequency-based model (k-ω) at the wall and (k-ε) model in the bulk flow. A blending function ensures a smooth transition between

the two models. The SST model has been shown to capture more effectively the amount of flow separation under an adverse pressure gradient than other eddy viscosity models; hence it can precisely predict the near-wall turbulence, an essential parameter for accurate prediction of turbulent heat transfer [3].

The STARCCM + software was used to generate the three-dimensional structured and unstructured grids. Fig. 6 shows the computational grid. A boundary layer region of locally structured grids was generated around the wall surfaces consisting of 15–25 layers of prismatic mesh as illustrated in Fig. 7. Setting the ratio of two adjacent grid sizes to nearly 1.2 allows fine grids near the solid walls. This choice enables the distance of the first grid point off a solid wall, measured in wall unit y^+, to be below 2 at nearly all locations in the viscous grid for all cases studied herein. Such condition is necessary for solving the viscous sublayer and heat transfer near the walls. Fig. 8 illustrates the distribution pattern of y^+ a circular hole with $\alpha = 45°$, $L = 5mm$. The exact definition of the y^+ value is given below:

$$y^+ = \frac{y}{\nu}\sqrt{\frac{\tau_w}{\rho}} \tag{21}$$

For computational accuracy, the ratio of two adjacent grid sizes in any direction was kept within 0.82–1.2 and the height of the first cell from the wall was $y = 1.5 \times 10^{-6} m$. The grid of the inclined hole was controlled by 80 FFD design variables of control points on ten cross-sections through the thickness of the wall, as illustrated in Fig. 2(b).

4.1.1. Mesh sensitivity analysis

To determine the proper mesh size as a tradeoff between the accuracy and the efficiency of computing the cooling effectiveness, a mesh sensitivity analysis was performed on three grids with different resolution. The characteristics of the three grids used to represent the flow domain are reported in Table 2, and the operating conditions of the simulations in Table 3. Fig. 9 illustrates the velocities and mass densities at different locations of the domain. Runs A, B and C correspond to the circular hole configuration depicted in Fig. 6 and are discretized respectively by the Coarse (C), Medium (M) and Fine (F) meshes (Table 2). The values of the discharge coefficient C_D and the blowing ratio are also reported in Table 2. C_D is related to the pressure difference ΔP between the secondary and primary channels. The blowing ratio $M = \rho_{jet} V_{jet} / \rho_{hot} V_{hot}$ where V_{jet} and ρ_{jet} are the bulk velocity and the mass density of the jet, and V_{hot} and ρ_{hot} are those of the hot stream. Finally, the density ratio is defined as $D_R = \rho_{jet}/\rho_{hot}$. The results of the three levels of grid indicate that the Medium (M) grid is sufficient to produce the main features of the flow here under investigation.

4.1.2. Setup of optimization cases

Table 4 summarizes the setups of the nine cases that study the effect of the initial design and inclination angle on the optimization results. Circular and elliptical in-plane hole shapes of prescribed area, widely used in industry, are adopted as initial designs for Case 1 to 4 and Case 5 to 9 respectively. The radius of the circular hole is $2.5 \times 10^{-4} m$, and the aspect ratio of the elliptical hole is 2 with $7.0 \times 10^{-4} m$ long major axis perpendicular to the flow direction.

The CFD models (STARCCM+) have satisfactory accuracy of the in-plane hole area with less than 0.97% error from the theoretical values. For Case 1 and 2, the inclination angle is prescribed at $\alpha \equiv 45°$, and only the coordinates of the control points for the shape boundary are variable. For Case 3 to 6, also the inclination angle is a variable with initial value $\alpha_0 = 45°$, and for Case 7 to 9, with initial value of 60°, 80° and 90° respectively. The reason for assigning dissimilar initial values is to gauge the dependence of the optimized results on α, obtained via a gradient-based optimizer. The constant area constraints are implemented through two inequalities (Eq. (6)) using relaxation parameters. We explore two options for the area constraint: $\varepsilon_1 = \varepsilon_2 = 0.05$ (Case 1, 3 and 5), and $\varepsilon_1 = 1.0, \varepsilon_2 = 0.05$ (other cases). For the latter, the lower bound on the area is $(1 - \varepsilon_1) = 0$, hence only the upper bound can be effective. Symmetry of the in-plane shape in the x-y plane is always enforced about the x-axis, as discussed in Section 2.2. A supportive parametric study of the elliptical in-plane hole with $\alpha = 15°, 20°, 30°$ up to 90° was also performed to investigate the relation between inclination angle and cooling effectiveness.

4.2. Optimization results

The optimization results of the nine cases reported in Table 4 are grouped into three sets. The first examines case 1 to 4 with results listed in Table 5 and visualized in Fig. 10 (temperature profile). The optimized shapes all resemble the letter "V" pointing to the downstream direction, which results in an increase of the cooling effectiveness above 120%. Case 2 has no effective lower bound on the shape area in comparison with Case 1, and the larger design space of Case 2 leads to a more efficient design with < 1% larger cooling effectiveness than Case 1. More interestingly, the optimized hole in Case 2 is even smaller by 4.79% in area from the initial design. For Case 3 and Case 4, an even larger design space is searched by updating both the shape geometry and the inclination angle. In this case, the optimized cooling effectiveness is even higher with more than 150% increase. The optimized shapes in Case 3 and 4 resemble that of Case 1, but their inclination angles are about 35° instead of 45°, illustrating the effect of the inclination angle on the results. As shown in the temperature distribution plots in Fig. 10, the optimized designs can generate a larger area of the hot wall with a higher cooling effectiveness than that of the circular hole.

The second set of results pertains to Case 5 and 6. The difference from the previous set is the initial shape of the void, in this case being elliptical as opposed to circular. The cooling effectiveness of the elliptical hole with $\alpha = 45°$ is 0.029, 58.1% higher than that provided by the circular one, making it a more efficient initial design. Fig. 11 shows the optimized shapes and temperature distributions. Numerical results are tabulated in Table 6. The optimized shapes resemble "V" shapes similar to those of Case 1 to 4, but much thinner: the arms of the "V" are longer, and the region near the vertex has shrunk. The low temperature region extends further downstream in Fig. 11 compared with Fig. 10. The values of the cooling effectiveness further increase, with more than 170% growth (area also increased by 5%, meeting the upper bound), and Case 6 is the best among Case 1 to 6. The change in inclination angle is minor in Case 5 and 6, a noteworthy difference from Case 3 and 4.

Tables 5 and 6 demonstrate that the change of shape and the improvement of the objective function are significant, and the implementation of the relaxed formulation of area constraints, especially setup with effective upper bound of area only, is also successful. The dependence on the initial design is manifest by the nature of the gradient-based algorithm.

The third set includes the result from Case 7 to 9, where we further examine the effect of the inclination angle on the optimized shape of the cooling hole. Fig. 12 and Table 7 summarize the results. In Case 7 to 9, the inclination angle is prescribed at 60°, 80° and 90° respectively, while the other conditions are those of Case 6. Compared with Case 6 with the maximum effectiveness of 0.087 at the inclination angle α near 45°, the values of the optimized cooling effectiveness for Case 7 to 9 are below by at least 33%. However, the percentages of improvement from the initial design of elliptical hole are much larger, and can be as high as 440% for Case 8 with the smallest initial cooling effectiveness. A comparison of the results between Cases from 6 to 9 demonstrates the cooling effectiveness of a given shape is very sensitive to the inclination angle, and $\alpha \leq 45°$ is favorable for the maximization of the cooling effectiveness. The optimized shapes in Case 7 to 9 are also noteworthy. Unlike V-shapes in Case 1 to 6, the optimized shapes are thicker and curvier in the middle. Specifically, the optimized shape of Case 9 in Fig. 12 resembles a "W" and the direction is flipped, with the wider side facing downstream.

The effect of inclination angle on cooling effectiveness is further investigated by running a parametric study of the cooling effectiveness

of the elliptical hole in Table 7 with the inclination angle (α) varying from 15° to 90°. Fig. 13 shows the curve of the cooling effectiveness (η) as a function of α. Inclination angles corresponding to relatively high values of η between 0.035 and 0.048 are in the range of [15°, 45°], consistent with our optimization results in Case 1 to 9. A smaller α creates a larger projected area of the hole along the flow direction for downstream cooling. Beyond that range, η descends sharply with the increase of α, reaches the minimum of ~0.004 at 80°, which is less than 10% of the peak value, and recovers to ~0.006 as α reaches 90°. The parametric study suggests that the value of the inclination angle also plays a key role in the maximization of film-cooling performance apart from the initial design shape.

As a summary of the main results of this study, the cooling performance (P_r) of the initial and optimized designs of nine cases are compared in Table 8. For a given area, the maximum P_r among the 14 designs is about 33 times of the minimum one, despite the 15% difference of the blowing ratio (M) and 100% of the discharge coefficient (C_D). Moreover, the standard circular hole has the largest M but the P_r is the 10^{th} out of 14. The optimized shapes of Case 1 to 4 achieve at least 265% increase of P_r over the circular hole. The largest percentage of increase in P_r is 647% in Case 8. The importance of the inclination angle is again demonstrated: a switch of α from 60° to 80° can generate more than 400% difference in P_r. The comparison suggests the improvement of the cooling performance is mostly due to the optimized shapes of the hole and the selection of the inclination angle. Since P_r is a normalized performance metric (Eq. (2)), Table 8 further demonstrates that the optimized designs (Case 1 to 6) can achieve enhanced cooling effectiveness using a smaller blowing ratio than their initial counterparts, hence making them more efficient. In addition, we note that the mass flow rate through the hole in Eq. (2) is not available in the adjoint solver, hence the cooling performance is not selected as the objective function.

To visualize the physics of the flow around the cooling hole, we examine two representative cases, i.e. case 6 and 9. Fig. 14 illustrates the vortex structure generated by the optimized shapes and the circular shape, here taken as baseline. The velocity vectors align with temperature contours in the y-z plane at $x = 3.0 \times 10^{-4}$, and show the formation of a couple of vortices downstream of the hole. As compared to the cylindrical hole, the optimized shapes yield a uniform velocity at the exit of the cooling hole, thus generating weaker anti-vortices. The benefit is an improved flow field that reduces the mixture between the main and the jet streams, and it increases the film-cooling effectiveness. Fig. 15 illustrates the temperature profiles of the circular hole, the elliptical hole and the optimized holes of Case 6 and Case 9. The profiles show that the optimal shape corresponding to Case 6 reduces the flow separation, thereby improving the cooling air attachment to the hot surface and enlarging the cooled downstream area.

Although the variables here examined, i.e. in-plane shape boundary and inclination angle, are effective in showing an increase in the cooling effectiveness, the results show a strong dependence on the initial values of the variable. This outcome is expected to a certain extent because it stems from the use of a gradient-based algorithm capable of finding local optima. Further work is required to systematically search for the optimal shape of a single inclined hole from various initial shapes. More importantly, other design factors can heavily influence the cooling performance of a given void shape. For a standalone hole, the rotation of the in-plane shape determines its projected area on the plane perpendicular to the inlet flow, a key factor related to the cooling effectiveness. Furthermore, cooling holes in gas turbine structures are usually deployed in a pattern for further improved performance through the interaction of holes. The effect of tessellation on cooling performance is worthy of future investigation. Our gradient-based framework has been conceived to handle an even larger number of design variables, and only requires an update of the numerical analysis module. If this causes a steep increase in the computational cost, other approaches can be considered, such as the overset method [16,17].

Another important aspect of the methodology that needs further improvement is the meshing module. The mesh deformation technique adopted herein can save the computational cost from remeshing, but it is not always robust. The mesh deformation module is able to handle small and sometimes medium size deformation, but it can pose problem with large deformation as the mesh may collapse. The mesh repair module can remedy no more than hundreds of collapsed volume elements. Close examination of failed examples of mesh update shows the difficulty usually occurs where high aspect ratio prismatic elements are connected to flat tetrahedral ones.

5. Conclusion

In this paper, the gradient-based shape optimization of low porosity film-cooling hole with two initial designs and various inclination angles is investigated for maximization of the cooling effectiveness. All optimized shapes can improve cooling effectiveness of more than 120% from circular and elliptical initial designs. Smaller inclination angle between 15° and 45° can create larger projected area of the hole for the best gain of cooling. Optimized shapes form a family of V-shapes that can be further validated by wind-tunnel tests. The automated workflow implemented in this work can be applied to other CFD-based shape optimization problems.

Declaration of competing interest

The authors declare that they have no known competing financial interests or personal relationships that could have appeared to influence the work reported in this paper.

Acknowledgement

The authors would like to acknowledge the financial support provided by Natural Sciences and Engineering Research Council of Canada Collaborative Research and Development Grant No. 242561. The authors also would like to thank Prof. Svanberg for providing the MATLAB code of MMA optimizer. The computational resources used to perform the data analysis were provided by CLUMEQ (http://www.clumeq.mcgill), which is funded in part by McGill University.

Appendix A. Supplementary data

Supplementary data to this article can be found online at https://doi.org/10.1016/j.ijthermalsci.2020.106542.

References

[1] B. An, J. Liu, S. Zou, Effects of mainstream turbulence intensity and coolant-to-mainstream density ratio on film cooling effectiveness of multirow rectangular diffusion holes, J. Heat Trans-T. ASME 141 (2019) 122001.
[2] W.K. Anderson, V. Venkatakrishnan, Aerodynamic design optimization on unstructured grids with a continuous formulation, Comput. Fluids 28 (1999) 443–480.
[3] J.E. Bardina, P.G. Huang, T. Coakley, Turbulence Modeling Validation, Testing, and Development, Technical Report 97N19942, NASA, 1997.
[4] F. Beux, A. Dervieux, Exact-gradient shape optimization of a 2-D Euler flow, Finite Elem. Anal. Des. 12 (1992) 281–302.
[5] D.G. Bogard, K.A. Thole, Gas turbine film cooling, J. Propul. Power 22 (2006) 249–270.
[6] P. Chen, L. Wang, X. Li, J. Ren, H. Jiang, T. Simon, Enhancement of film cooling effectiveness using Dean vortices, J. Turbomach. 142 (2020), 011005.
[7] Z. Chi, H. Liu, S. Zang, Geometrical optimization of nonuniform impingement cooling structure with variable-diameter jet holes, Int. J. Heat Mass Tran. 108 (2017) 549–560.
[8] M. Giles, N. Pierce, An introduction to the adjoint approach to design, Flow, Turbul. Combust. 65 (2000) 393–415.
[9] N.A. Gumerov, R. Duraiswami, Fast radial basis function interpolation via preconditioned Krylov iteration, SIAM J. Sci. 29 (2007) 1876–1899.
[10] E. Iuliano, E. Andres-Perez, Application of Surrogate-Based Global Optimization to Aerodynamic Design, Springer International Publishing, Cham, 2016.
[11] A. Jameson, S. Kim, Reduction of the adjoint gradient formula in the continuous limit, in: Proc. 41th Aerospace Sciences Meeting and Exhibit, 2003.

[12] K.D. Lee, K.Y. Kim, Shape optimization of a fan-shaped hole to enhance film-cooling effectiveness, Int. J. Heat Mass Tran. 53 (2010) 2996–3005.
[13] K.D. Lee, K.Y. Kim, Surrogate based optimization of a laidback fan-shaped hole for film-cooling, Int. J. Heat Fluid Flow 32 (2011) 226–238.
[14] G. Li, P. Yang, W. Zhang, Z. Wu, Z. Kou, Enhanced film cooling performance of a row of cylindrical holes embedded in the saw tooth slot, Int. J. Heat Mass Tran. 132 (2019) 1137–1151.
[15] W. Li, X. Lu, X. Li, J. Ren, H. Jiang, On improving full-coverage effusion cooling efficiency by varying cooling arrangements and wall thickness in double wall cooling application, J. Heat Trans-T. ASME 141 (2019), 042201.
[16] A. Madrane, Parallel implementation of a dynamic overset unstructured grid approach, in: C. Groth, D.W. Zingg (Eds.), Proc. 3rd International Conference on Computational Fluid Dynamics, Springer Science & Business Media, 2004, pp. 733–739.
[17] A. Madrane, A. Raichle, A. Stuermer, Parallel implementation of a dynamic unstructured chimera method in the DLR finite volume tau-code, in: M. Khalid, S. Chen, S. Mcilwain (Eds.), Proc. 12th Annual Conference of the CFD Society of Canada, CFD Society of Canada, 2004, pp. 524–534.
[18] F. Menter, Two-equation eddy-viscosity turbulence models for engineering applications, AIAA J. 32 (1994) 1598–1605.
[19] A. Moeini, M.R. Zargarabad, Genetic algorithm optimization of film cooling effectiveness over a rotating blade, Int. J. Therm. Sci. 125 (2018) 248–255.
[20] J. Nocedal, S. Wright, Numerical Optimization, Springer Science & Business Media, New York, 2006.
[21] G. Nowak, W. Wroblewski, Optimization of blade cooling system with use of conjugate heat transfer approach, Int. J. Therm. Sci. 50 (2011) 1770–1781.
[22] S. Park, E.Y. Jung, S.H. Kim, H.S. Sohn, H.H. Cho, Enhancement of film cooling effectiveness using backward injection holes, Int. J. Therm. Sci. 110 (2016) 314–324.
[23] P.L. Roe, Approximate Riemann solvers parametric vectors and difference schemes, J. Comput. Phys. 42 (1981) 357–372.
[24] J.A. Samareh, Survey of shape parameterization techniques for high-fidelity multidisciplinary shape optimization, AIAA J. 39 (2001) 877–884.
[25] G.R. Shubin, P.D. Frank, A Comparison of Two Closely-Related Approaches to Aerodynamic Design Optimization, Technical Report 92N13933, NASA, 1991.
[26] S.N. Skinner, H. Zare-Behtash, State-of-the-art in aerodynamic shape optimisation methods, Appl. Soft Comput. 62 (2018) 933–962.
[27] J.C. Spall, Introduction to Stochastic Search and Optimization: Estimation, Simulation, and Control, John Wiley & Sons, Hoboken, 2005.
[28] K. Svanberg, The method of moving asymptotes—a new method for structural optimization, Int. J. Numer. Methods Eng. 24 (1987) 359–373.
[29] K. Svanberg, MMA and GCMMA - Two Methods for Nonlinear Optimization, 2007.
[30] C. Wang, J. Zhang, J. Zhou, Optimization of a fan-shaped hole to improve film cooling performance by RBF neural network and genetic algorithm, Aero. Sci. Technol. 58 (2016) 18–25.
[31] G. Xie, Y. Song, B. Sunden, Computational optimization of the internal cooling passages of a guide vane by a gradient-based algorithm, Numer. Heat Tr. A-Appl. 69 (2016) 1311–1331.
[32] G. Zhang, J. Liu, B. Sunden, G. Xie, On the improvement of film cooling performance using tree-shaped network holes: a comparative study, Numer. Heat Tr. A-Appl. 74 (2018) 1121–1138.